aerospace

MDPI

Article

Experimental Study on the Water Content Distribution of Profile Samples and the Improvement of Sampling Detection Methods

Ye Tian [1], Jiahang Zhang [1], Junyue Tang [2,*], Wei Xu [1], Weiwei Zhang [2,*], Lijun Tao [2], Shengyuan Jiang [2] and Yanbin Sun [1]

[1] School of Light Industry, Harbin University of Commerce, No. 1, Xuehai St., Songbei Dist., Harbin 150028, China; tian8154@126.com (Y.T.); zjhang15545175157@163.com (J.Z.); hljhrbxw@163.com (W.X.); atlantisity@163.com (Y.S.)

[2] School of Mechanical and Electrical Engineering, Harbin Institute of Technology, No. 92, Xidazhi St., Nangang Dist., Harbin 150006, China; 18846780409@163.com (L.T.); jiangshy@hit.edu.cn (S.J.)

* Correspondence: tangjunyue@hit.edu.cn (J.T.); zweier@hit.edu.cn (W.Z.)

Abstract: To provide reliable input information for the load design and extraction of lunar soil water ice samples, it is necessary to study the water content distribution and water migration of simulated lunar soil water ice samples. On this basis, the temperature field model and the hydrothermal coupling relationship are proposed. The temperature field model was constructed by combining energy conservation and Fourier's heat transfer law. The coupling relationship was established, and the hydrothermal coupling model was obtained by testing the unfrozen water content using the nuclear magnetic resonance method. Finite element software was used to solve the model numerically, and the water migration rule of the soil water ice samples at different ambient temperatures were analyzed. Thin-wall drilling tests were carried out on the simulated lunar soil water ice samples to obtain water content data for different locations, and the simulation results were verified. Due to the migration effect of the cold end of the water, the closer we tested to the edge of the sample, the higher the water content was. The higher the ambient temperature was, the more pronounced the water migration phenomenon of the whole sample was. These research results provide a basis for sampling scheme design.

Keywords: lunar soil water ice sample; water migration; hydrothermal coupling model; thin-wall drilling test; cold end migration effect

Citation: Tian, Y.; Zhang, J.; Tang, J.; Xu, W.; Zhang, W.; Tao, L.; Jiang, S.; Sun, Y. Experimental Study on the Water Content Distribution of Profile Samples and the Improvement of Sampling Detection Methods. *Aerospace* **2023**, *10*, 635. https://doi.org/10.3390/aerospace10070635

Academic Editor: M. Reza Emami

Received: 18 March 2023
Revised: 30 June 2023
Accepted: 5 July 2023
Published: 14 July 2023

1. Introduction

Scientific loads for in situ exploration should be designed based on the mechanical, thermal, and electrical properties of lunar soil water ice. However, the difference in water distribution in simulated lunar soil water ice samples and additional unknown deviations in the test results of samples and feedback information under different target points affect the analysis results of test data. Therefore, it is necessary to explore the law of water migration of lunar soil water ice samples during the freezing process to ensure the specific water content requirements of the samples extracted and the accuracy of the test results.

The amount of near-surface water released into the outer layers of the Moon can be detected by probing the response of water molecule abundance to fluctuations in its 18 water channels per charge mass via neutral mass spectrometry (NMS) [1]. The water content of ice in soil was assessed using NMR methods to manipulate the decay rate of H-nucleation in water by means of an external magnetic field [2]. The alternating stratification of ice and soil layers was discovered as early as 1930 in an open system experiment [3]. The capillary theory can explain the driving form of this phenomenon [4]. Measuring the movement of a frozen front in frozen soil through the ray attenuation method and calculating the change

in chemical potential in the frozen soil, it was observed that its migration is based on an unfrozen water film under the action of a temperature gradient [5]. The measuring device for the characteristics of water migration in saturated frozen soil can be used to explore the influence of temperature gradient on the level of migration and water recharge [6]. The freezing process of frozen soil is divided into the early stage and the late stage, and the whole sample is divided into upper and lower layers. In one study, the upper layer of frozen soil always showed an increasing trend at the beginning of freezing and gradually decreased in the second half, while the opposite was true for the lower layer [7]. The finding in this study on volatile matter measurement was that the simple addition of liquid water to the simulation resulted in soil agglomeration, which prevented water from being evenly distributed throughout the sample [8]. A preliminary analysis of the means of affecting water migration found that migration in vapor and liquid forms was predominant, while the migration of solid forms occurred when external loads were applied. The mineral particle diameter, water supply conditions, and cold source temperature affect the degree of water migration [9]. By studying the migration characteristics of water in undisturbed soil and soil reshaped during the freezing–thawing process, we found that cracks and water accumulation occurred under the same conditions, and the greater the initial water content was, the greater the accumulation was [10]. Through a correlation analysis between the unfrozen water content and temperature in frozen soil, a hydrodynamic hydrothermal coupling model applicable to the frozen soil field was established. However, this solution is difficult to implement due to limited means [11]. Based on Fick's law, a water–thermal coupling model for chalk and sand soils was experimentally constructed and calibrated to predict the coupling of heat and moisture in soils at transient boundary temperatures [12]. Constructing a larger-scale migration test device, it was clear that the influence of temperature potential during moisture migration is relatively weak in a study where the phenomenon of layered ice coalescence was analyzed and the moisture field was coupled with the temperature field based on the finite element method to provide a basis for frost heave control [13]. Other authors built a frost-heaving model containing external loads to solve the inadequacy of the Harlan model for frost heaving caused by water migration [14]. In this study, we mainly studied the water content distribution of simulated samples of lunar soil water ice, established a temperature model through heat transfer mechanism and the energy conservation law, and tested the dynamic parameters and supplementary conditions to be set for the model through corresponding experiments, thus obtaining a hydrothermal coupling model. The heat and water distribution of lunar soil water ice samples under different temperature conditions were obtained by solving the hydrothermal coupling model through simulation analysis. Finally, the simulation analysis results were verified using sampling tests with thin-wall drilling.

2. Construction of Temperature Field Model and Coupling Equation

2.1. Construction of Temperature Field Model in Sample Freezing Process

The variation in the water component field in the freezing process is based on the driving force of the temperature field. The construction of the temperature field is similar to that of the water field. This paper describes the temperature field based on the Fourier heat transfer law and energy conservation relationship. A temperature field model was constructed considering the effect of latent heat on heat change.

Based on the Fourier heat transfer principle, the expression of heat flux q can be seen in Equation (1):

$$q = -\lambda\left(\frac{\partial T}{\partial x} + \frac{\partial T}{\partial y}\right) \tag{1}$$

where T is the temperature of the microelement (K) and λ is the thermal conductivity coefficient of the sample (W/(m·k)). From the perspective of water variation in the microelement, it can be seen that part of the heat absorbed by the microelement is used to change the

temperature of the microelement, and the other part is used to balance the latent heat of the phase transition between the water and ice. The equilibrium equation is shown as follows:

$$C_p \frac{\partial T}{\partial t} = \lambda\left(\frac{\partial^2 T}{\partial x^2} + \frac{\partial^2 T}{\partial y^2}\right) + \left(\frac{\partial \lambda}{\partial x} + \frac{\partial \lambda}{\partial y}\right)\left(\frac{\partial T}{\partial x} + \frac{\partial T}{\partial y}\right) + L\rho_i \frac{\partial \theta_i}{\partial t} \quad (2)$$

where C_p is the volumetric heat capacity of the sample, ρ_i is the density of ice, θ_i is the volumetric ice content of the sample element, and L is the latent heat of phase transformation (J/kg).

The governing equations of the water field and temperature field can be obtained based on the Fourier heat transfer principle and the micro-element heat balance equation. With the introduction of the Hamilton operator $\nabla = \frac{\partial}{\partial x} + \frac{\partial}{\partial y}$, the equation can be summarized as follows:

$$\begin{cases} \frac{\partial \theta_1}{\partial t} + \frac{\rho_i}{\rho_1}\frac{\partial \theta_i}{\partial t} = \nabla[k(\theta)\nabla(\psi)] \\ C_p \frac{\partial T}{\partial t} = \nabla[\lambda \nabla(T)] + L\rho_i \frac{\partial \theta_i}{\partial t} \end{cases} \quad (3)$$

where λ is the comprehensive thermal conductivity coefficient; θ_1 and θ_i are the saturated volume moisture content and volume ice content for the sample, respectively; and ρ_i is the density of ice. The presence of three dependent variables, θ_1, θ_i, and T, for the three independent variables x, y, and t resulted in no solution to the control equation. Therefore, the coupling relationship between the moisture field and the temperature field needs to be considered.

2.2. Determination of Unfrozen Water via Nuclear Magnetic Resonance

To establish the coupling relationship between the water field and the temperature field and identify the main temperature interval of water migration, it is necessary to test the unfrozen water content in the samples. In this study, the unfrozen water content in samples at different temperatures was tested using the nuclear magnetic resonance method to quantitatively express the relationship between the unfrozen water and temperature in the model element.

(1) Test equipment composition and temperature control principle.

The NMR instrument used in this experiment is shown in Figure 1, which mainly comprises a temperature control system, test system, and data acquisition system. The controllable temperature of the system itself can be as low as −30 °C. In this study, the minimum required temperature was −196 °C, and the temperature control box could control the samples within the temperature range of −80 °C–30 °C. In the temperature range of −80 °C to −196 °C, the samples need to be cooled using liquid nitrogen. The whole sample was placed in an insulated sample barrel. In order to prevent the disturbance of the simulated sample caused by the insertion of the temperature sensor probe into the simulated sample, it is necessary to prepare the samples with the same conditions as the simulated sample, i.e., the companion parts, and place them in the same environment with the simulated sample. The temperature sensor can reflect the temperature of the real simulated sample by detecting the temperature of the companion parts. A liquid nitrogen bath was used for this process. The results are shown in Figure 2. With the help of the thermal insulation characteristics of the sample barrel, the high heat flux caused by the large temperature difference was weakened, thus slowing down the overall temperature drop rate. Due to the high test efficiency of the nuclear magnetic resonance device, the temperature fluctuation was small, meeting the test requirements.

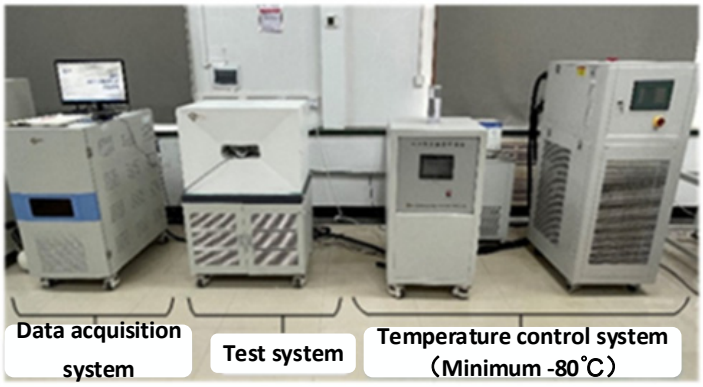

Figure 1. Nuclear magnetic resonance instrument.

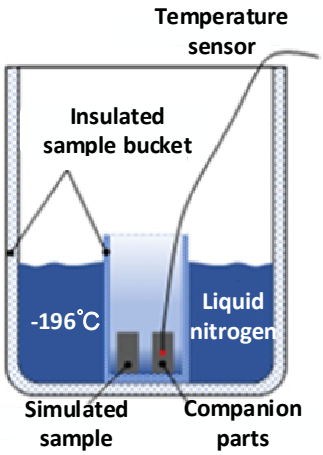

Figure 2. Extremely low-temperature drop system.

(2) Test process and parameter design.

The prepared water-containing simulated lunar soil was placed in the sample container, and the sample was cooled down in a gradient using a low-temperature temperature control box and liquid nitrogen. Subsequently, the temperature of the sample was controlled through the insulation bucket. When the temperature of the sample reached the point to be measured, it was quickly taken out for testing.

In this experiment, the dry density range of 1.30–1.70 g/cm^3 was selected, and the mass moisture content of the samples was controlled at 5% and 10%, respectively. Research shows that the most drastic change in the moisture content of a sample ranges from −5 °C to 0 °C; thus, the layout of the temperature measuring points was assigned the most focus here, with an overall normal distribution. The acquisition of the temperature points in the normal temperature range and the extremely low-temperature range was reduced, and 22 temperature measuring points were finally selected (20 °C, 15 °C, 10 °C, 5 °C, 2 °C, −0.2 °C, −0.5 °C, −2 °C, −3 °C, −4 °C, −5 °C, −9 °C, −15 °C, −20 °C, −30 °C, −50 °C, −80 °C, −100 °C, −130 °C, −150 °C, −180 °C, −196 °C).

(3) Analysis of test results.

Deviation occurs in the preparation process of samples. The final sample dry density distribution is shown in Table 1, and the volume moisture content can be calculated accordingly. By analyzing the characteristics of the paramagnetic curve, the linear fitting formula of the paramagnetic curve can be obtained based on the distributed scatter data as follows:

$$A = -0.09T + 511.5 \quad (4)$$

where A is the strength of the nuclear magnetic signal (a.u), and T is the sample temperature (°C).

Table 1. Distribution of sample density and water content.

Number	NMR-1	NMR-2	NMR-3	NMR-4	NMR-5	NMR-6	NMR-7	NMR-8
Density (g/cm^3)	1.29	1.35	1.39	1.43	1.55	1.59	1.61	1.70
Moisture content (%)	12.9	6.75	13.9	7.15	7.75	15.9	16.1	8.50

According to the analysis of the test results, it can be concluded that the change in unfrozen water content presents the following characteristics:

The change in unfrozen water content presents a zonal feature, and the initial moisture content with the obvious difference of 10% was used for analysis. The variation in the mass moisture content of the samples with temperature for different dry densities is shown in Figure 3. According to the distribution characteristics of the moisture content, the whole process of change is divided into four main regions. The right side of 0 °C is the subcooling stage. In this region, the nuclear magnetic signal intensity changes with the decrease in temperature, but the actual water content does not change. Therefore, the positive temperature area in this section should be approximated as a straight line. Then, the rapid freezing stage occurs around −30 °C to 0 °C with a linear decrease in the water content, followed by a gradual stabilization. After the slow freezing stage, the stable freezing stage occurs.

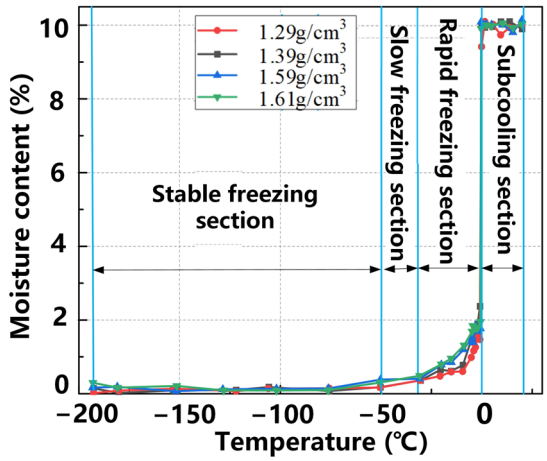

Figure 3. Moisture content changes with temperature under different dry densities.

2.3. Construction of Hydrothermal Coupling Model

The coupling relation is the key to supplementing the solution of the above hydrothermal coupling equation. The coupling relation adopted in this paper is based on the relation between the unfrozen water content and temperature, and the influence of the unfrozen water content on the sample dry density and initial volume water content should be considered. Therefore, it is necessary to build a hydrothermal coupling model of lunar soil water ice considering the effects of the initial volume water content and dry density and perform linear fitting to obtain the final unfrozen water content distribution model with the relationship between the initial volume water content A, sample dry density S, and temperature D, as shown in Equation (5):

$$\theta_u = \begin{cases} \frac{\rho_s(1-\theta_s)}{100\rho_w}\alpha(-T)^\beta & T < T_f \\ \theta_0 & T > T_f \end{cases} \quad (5)$$

where α and β are the fitting parameters of the model; θ_s is the saturated volume moisture content of the sample; ρ_s is the dry density of the sample (g/cm^3); and ρ_w is the density of water at room temperature (g/cm^3). In the process of processing the fitting curve, it is found that the fitting parameters α and β in the unfrozen water content model are linearly correlated with the initial volume of the water content. $\alpha = -18.7402\theta_0 + 1.0421$ and

$\beta = -6.1989\ \theta_0 + 0.1456$. Equation (5) is the hydrothermal coupling relationship connecting the water and temperature fields. Therefore, the hydrothermal coupling model for the water migration problem of lunar soil water ice during gradient refrigeration is complete. The three variables correspond to three equations, and the model can be solved.

3. Analysis of the Hydrothermal Characteristics of Omnidirectional Frozen Samples

3.1. Temperature Characteristics of Omnidirectional Frozen Samples

The temperature distribution of the simulated samples in the omnidirectional freezing process was analyzed. Compared with the unidirectional freezing method, the initial setting of thermal boundary conditions needs to be changed. In addition, the two-dimensional axisymmetric model is more suitable for studying sample conditions, which has a faster solution speed than simple two-dimensional conditions. The grid division and boundary conditions of the model are shown in Figure 4.

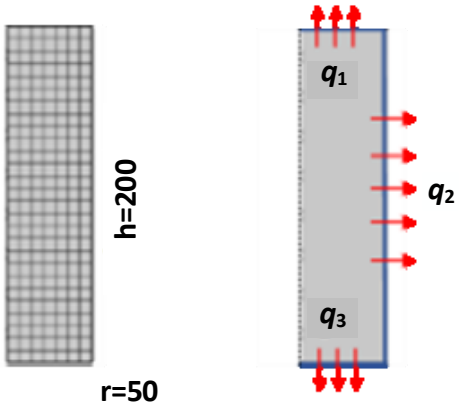

Figure 4. Grid and boundary diagram.

3.2. Water Characteristics of Omnidirectional Frozen Samples

According to the above setting of the thermal boundary conditions of the simulated samples, the simulated samples were placed in an omnidirectional freezing environment in which the heat transfer characteristics and temperature distribution conditions affected the water distribution. The final three-dimensional view of the water distribution of the output samples is shown in Figure 5.

(1) There is a "shell" region: The macroscopic distribution of moisture shows that the outer wall of the sample forms a "shell"-like structure at different cold source temperatures. This thin layer is the main zone of moisture increase, while the corresponding inner "core"-like structure exists, which is the main zone of moisture decrease.

(2) The cryogenic zone advances in a ring: The freezing process can be summarized as the four main stages shown in Figure 6. In freezing stage 1, the lowest temperature point appears at the bottom corner. There are two directions of cold input here, which first cause freezing, and the water migrates to this location. With time, the dark part of the water decreases and shows a circular trend, which will also be the direction of subsequent water migration. As the low-temperature area advances to the center in a "ring"-like manner, the water freezing will inevitably present the corresponding characteristics, as shown in stage 3. As the water decreases, the water will be replenished in the central area.

The simulated slice analysis of the sample is shown in Figure 7. The sample was cut into 10 sections in the axial direction with a thickness of 20 mm to explore the distribution characteristics of the axial water content. Similarly, the samples were divided in the radial direction, and the radii of each layer were r_1 = 60 mm, r_2 = 45 mm, r_3 = 35 mm, r_4 = 25 mm, r_5 = 15 mm, and r_6 = 5mm, and the variation characteristics of the radial water content were analyzed.

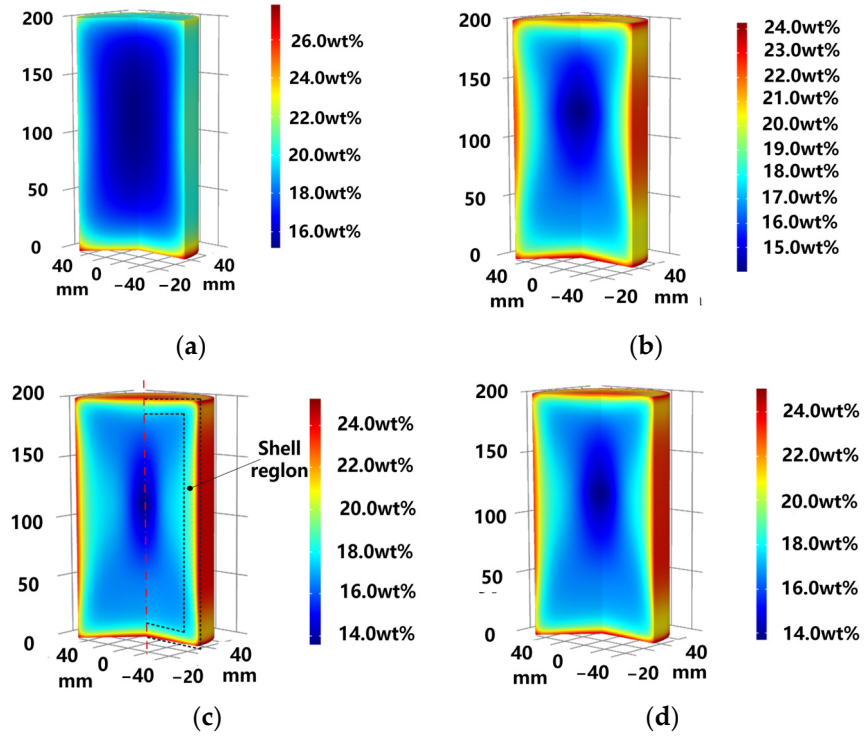

Figure 5. Sample water distribution. (**a**) Cold source temperature −10 °C. (**b**) Cold source temperature −30 °C. (**c**) Cold source temperature −50 °C. (**d**) Cold source temperature −80 °C.

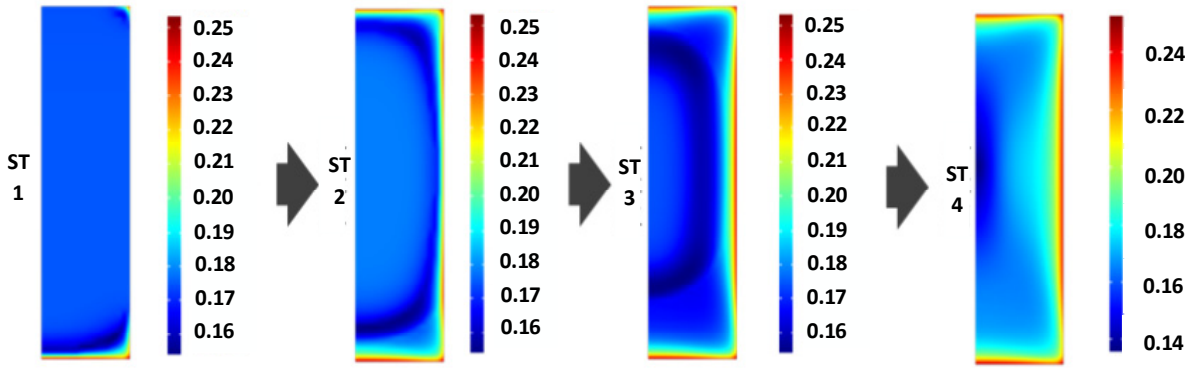

Figure 6. Freezing process schematic.

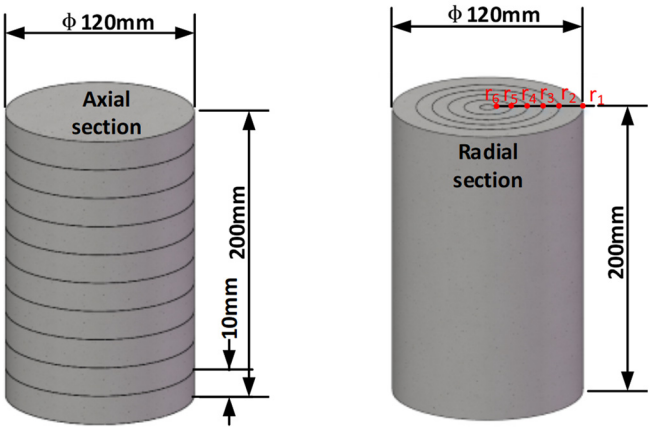

Figure 7. A 3D schematic diagram of a sample simulation section.

Figure 8 shows the change in axial water content. Under different cold source temperatures, the two cold source directions are still the main directions of water migration. Similar to the unidirectional freezing test, the water migration phenomenon is more obvious under higher cold source temperatures. The area with the most drastic change in the water is approximately 30 mm away from the cold source. The uneven distribution of water in the middle is also very strong at −10 °C. In contrast, the radial distribution of the water is shown in Figure 9. The macroscopic distribution tends to migrate toward the cold source, but the radial size is smaller than the axial size, making the variability between working conditions relatively small.

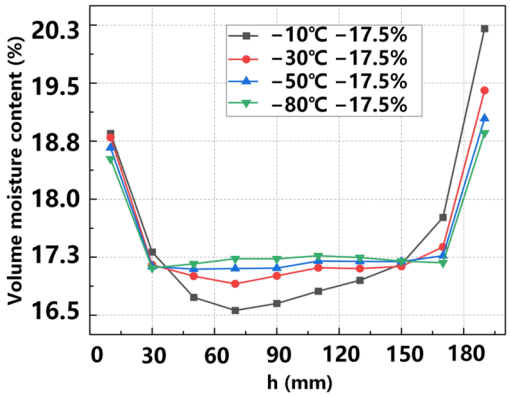

Figure 8. Distribution of axial water slices.

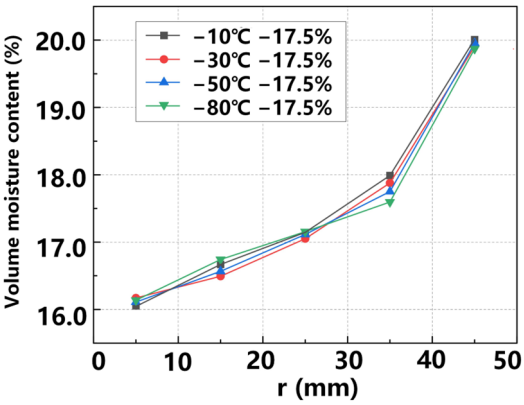

Figure 9. Radial moisture distribution in layers.

4. Sampling and Detection Test of Profile Samples

4.1. Drilling Sampling to Detect Sample Water Loss

(1) Test equipment selection and scheme design.

The sampling drill bit was used as the main sampling tool in this experiment. The upper surface of the prepared simulated lunar soil water ice sample was drilled with a reaming drill bit. After drilling to a certain depth, the circular thin-wall sample was taken out. The sampling schematic diagram is shown in Figure 10.

In order to explore the distribution law of the water content of the whole sample, it is necessary to sample different points of the whole sample. Through drilling sampling at different points of the whole sample, the water content at different positions of the sample was measured to speculate the water content distribution of the whole sample. The drilling locations of the entire sample are shown in Table 2.

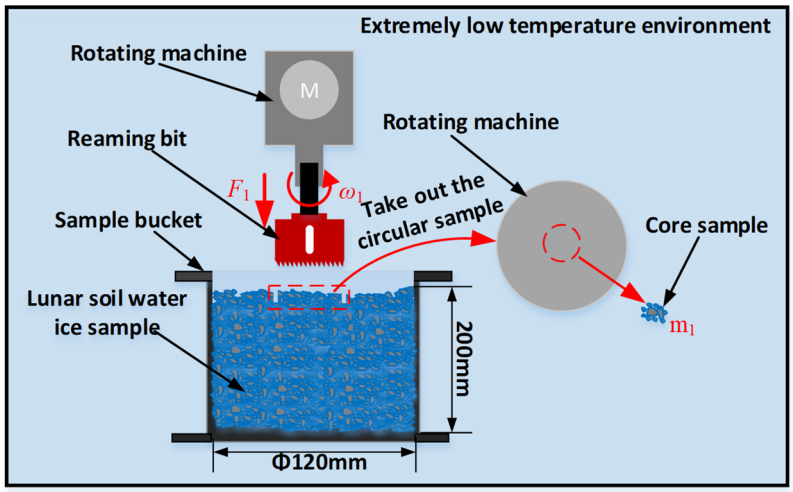

Figure 10. Schematic diagram of drilling and sampling.

Table 2. Grouping of test drilling points.

Number of Test Groups	Distribution Mode	DRILL POINT DISTRIBUTION
The first group	Axial distribution	Drilling depth: ① 10 mm; ② 60 mm; ③140 mm; ④ 200 mm.
The second group	Radial distribution	Distance from the center: ① 30 mm; ② 35 mm; ③ 40 mm; ④ 45 mm; ⑤ 50 mm.

The whole sample was drilled at different points to obtain the distribution rule of the water content of the whole sample. The whole drilling test scheme is shown in Figure 11. After each drilling, the middle position at the bottom of the whole cylindrical sample block was selected as the sampling detection point for water content detection.

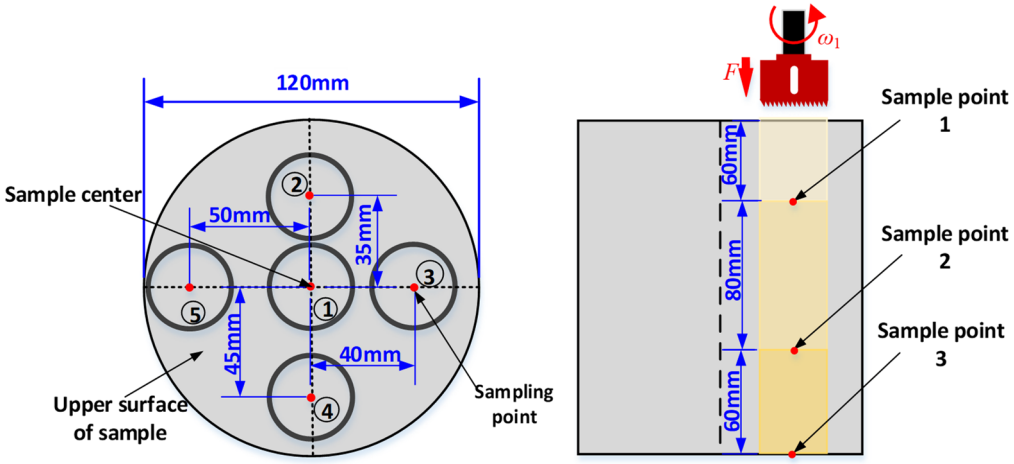

Figure 11. Schematic diagram of layered sampling.

The drilling, extraction, and weighing process of the entire sample is shown in Figure 12.

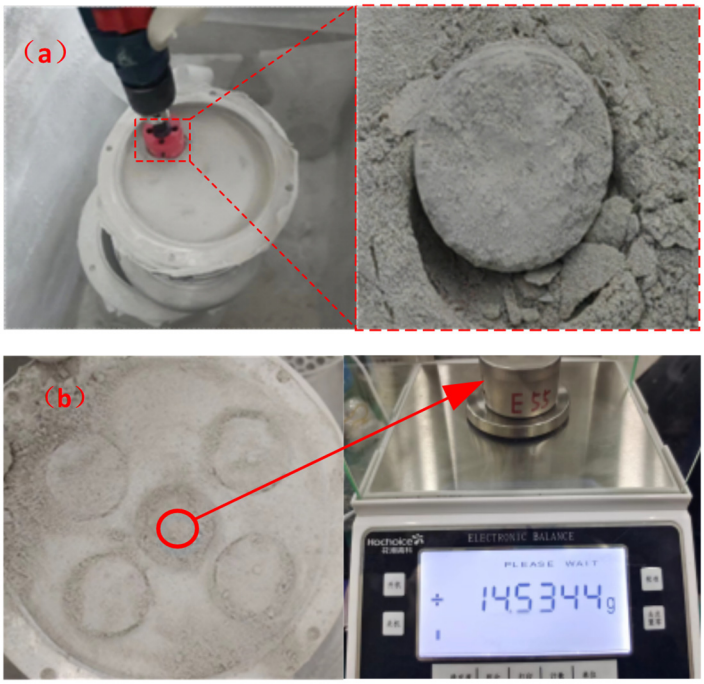

Figure 12. Sample drilling, extraction, and weighing. (**a**) Sample drilling. (**b**) Sample extraction.

After weighing, the moisture content of the sample was calculated using the thermogravimetric method.

In order to estimate the moisture distribution of samples under different temperature conditions, the drilling test was carried out in a −30 °C refrigerator and a −85 °C ultra-low-temperature refrigerator, and the drilling test was carried out at different points at two temperatures, respectively.

4.2. Comparative Analysis of Test Results and Simulation

(1) Influence of sample temperature on moisture content.

Figure 13 shows the test results generated through group tests conducted by setting different bit sizes and drilling rate parameters.

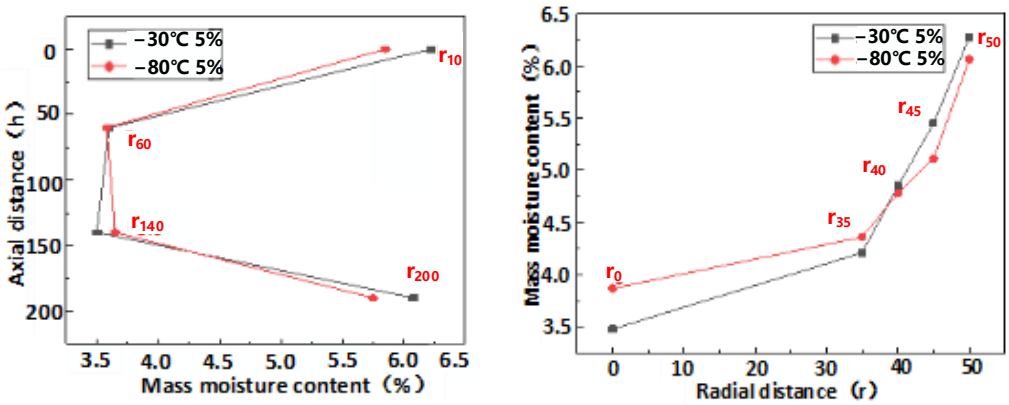

(**a**) (**b**)

Figure 13. Results of drilling test. (**a**) Axial water slice distribution. (**b**) Radial moisture distribution.

Figure 13a shows that the volume moisture content of the samples in the axial direction at the top detection point and the bottom detection point is higher than the original moisture content by 5.7%. The highest point's moisture content is 6.22%, and the lowest

water contents of the samples at the axial depths of 60 mm and 140 mm are 3.7% and 3.5%, respectively.

Figure 13b shows the radial water distribution of the whole sample. The water content of the five sample points is $r_0 < r_{35} < r_{40} < r_{45} < r_{50}$. As the radial distance gradually increases, the volume of the water content of the whole sample gradually increases. When the radial distance r = 0 mm, the moisture contents of the sample point are 3.5% and 3.8% at the lowest point, and the maximum value is 6.27% when the radial distance r = 50.

As shown in Figure 13a, the moisture content of the highest point is 6.22%, and that of the lowest point is 3.5%, with a difference of 2.72% at −30 °C. At −80 °C, the content of the highest point is 5.8%, and that of the lowest point is 3.53%, with a difference of 2.27%. Figure 13b shows that the difference in moisture content at the sampling points is 2.79% at −30 °C and 2.19% at −80 °C. According to the above data, the higher the ambient temperature of the sample is, the greater the difference in the entire water content is.

The water content distribution of the whole sample should be consistent with the trend of the broken line in Figure 13, and the fitting curve should be made according to all the data points in Figure 13. The trend of the fitting curve should be consistent with that of the water content of the whole sample. The average water content is the average value of the water content of the sample at −30 °C and −80 °C. The change law of the water content of the whole sample was analyzed with the increase in the radial and axial distance. The curve of the water content is shown in Figure 14.

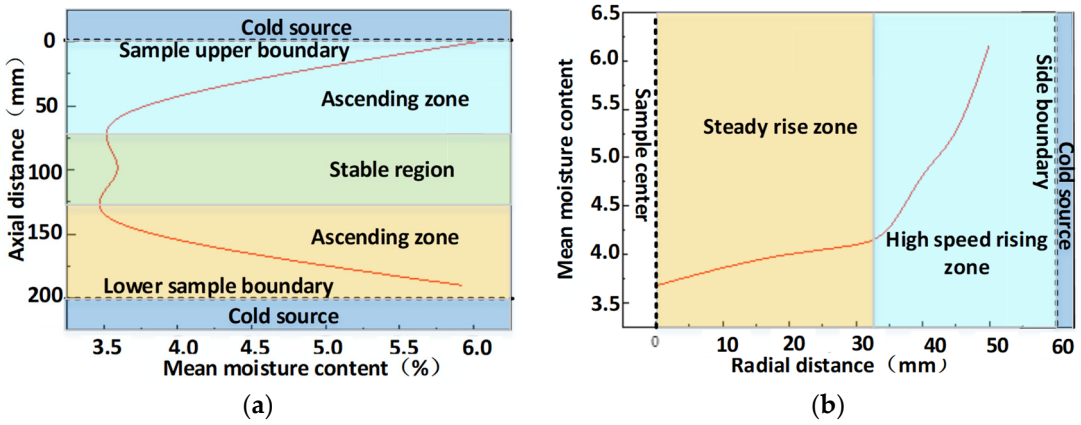

Figure 14. Variation in sample moisture content. (**a**) Axial water distribution. (**b**) Radial moisture distribution.

According to the above variation in the volume water content in axial and radial directions, it can be seen that:

1. According to Figure 14a, when the axial distance of the samples gradually increases, the average moisture content of the whole sample first decreases at high speed, subsequently becomes stable in the middle, and rises rapidly at the bottom.
2. From the perspective of radial direction, since the water content of the five sampling points in Figure 14 all increases with the increase in the distance from the sample center, it is inferred that the trend of the water content of the whole sample is as shown in Figure 14b. As the radial distance of the whole sample increases, the water content of the sample shows a gradually increasing trend. In the area near the center, the increasing trend of the sample moisture content is relatively stable, while near the measurement boundary, the sample moisture content is in a high-speed rising area, and the rising rate of the moisture content gradually increases.
3. Figure 14a,b shows that the sample moisture content near the upper and lower boundaries and the side boundary changes significantly, and the water content of the sample at the boundary is higher.

(2) Comparative analysis with simulation results.

In order to explore the similarity between the test results and the simulation results, it is necessary to calculate the average water content of each drilling sample at different temperatures and compare the test results of this test with the simulation results. The comparison of the data results is shown in Figures 15 and 16.

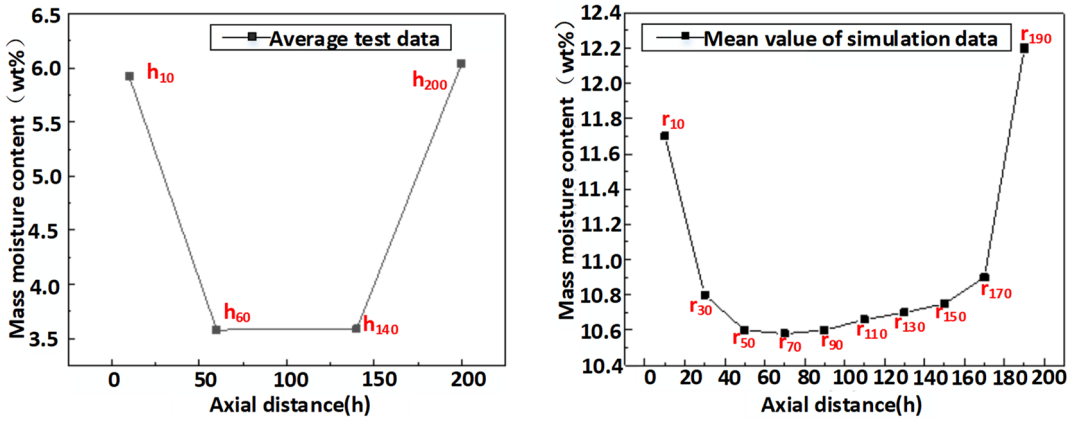

(**a**) (**b**)

Figure 15. Comparison of Drilling Axial Data; (**a**) Test data; (**b**) Simulation data.

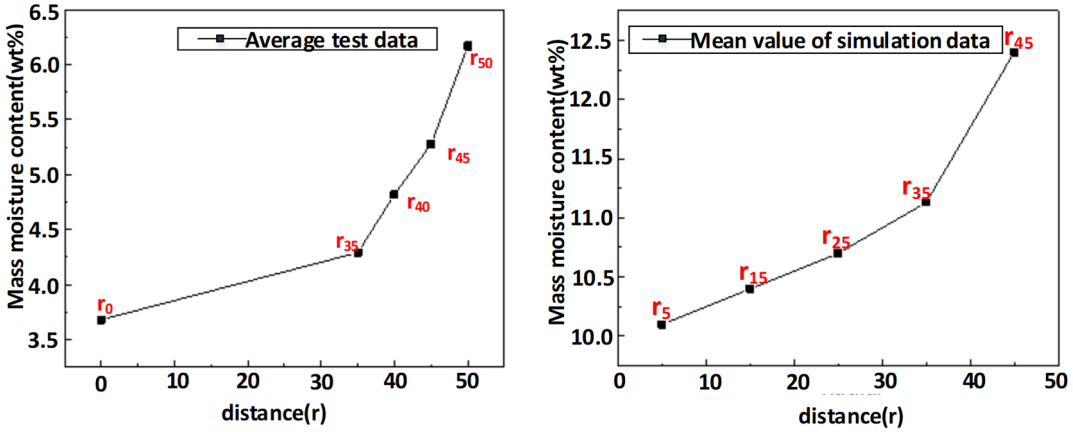

(**a**) (**b**)

Figure 16. Comparison of drilling radial data. (**a**) Test data. (**b**) Simulation data.

The data points in Figure 15a,b are the average test and simulation data of the axial moisture content of the samples. In Figure 15, with the increase in the depth of the test point, the volume of the water content of the whole sample first decreases and then increases, and the trend of the simulation data is similar to that of the test data. The data points in Figure 16a,b are the experimental and simulation data of the radial water content of the sample. It can be seen from Figure 16 that the mean value of the test data and the mean value of the simulation data have a similar variation, and the volume water content of the sample sampling point increases with the increase in the distance between the sampling point and the sample center. The sample water migrates in the direction of the sample boundary close to the cold source, and the closer the measured sample point is to the cold source, the higher the volume of the water content is.

5. Conclusions

In this study, based on the hydrothermal coupling model, the water content distribution and water migration rule of all the water-bearing simulated lunar soil samples under the omnidirectional freezing condition were simulated and analyzed. The results were verified through experiments. The following conclusions were obtained:

(1) When drilling the simulated lunar soil water ice samples at different points through thin-wall drilling, the water content distribution law of the simulated lunar soil samples was obtained, and the simulation results were verified. The water content of the simulated lunar soil samples was mainly distributed at the edge of the sample, and the closer we tested to the edge of the sample, the higher the water content of the sample was, indicating that the water in the whole sample had a migration effect towards the cold end.

(2) The temperature has a certain influence on the water migration effect of the whole sample, and the degree of water migration is more significant at a higher-boundary cold source temperature.

(3) According to the water distribution of the whole sample, the closer the sample is to the cold source, the less uniform the water content distribution is.

Author Contributions: Conceptualization: Y.T., J.Z. and L.T.; methodology: Y.T., J.Z. and L.T.; data collection: Y.T., J.Z. and L.T.; data maintenance: J.Z. and L.T.; formal analysis: J.Z. and L.T.; writing—original draft preparation: Y.T. and J.Z.; investigation: J.Z., L.T. and Y.S.; writing—review and editing: Y.T. and W.X..; supervision: Y.T. and J.T.; project administration: Y.T. and J.T.; visualization: J.Z.; funding acquisition: Y.T.; software: L.T., W.X. and Y.S.; resources: J.T., W.Z. and S.J.; writing—original draft preparation: J.Z., J.T. and W.Z.; writing—review and editing: L.T., S.J. and Y.S. All authors have read and agreed to the published version of the manuscript.

Funding: This research was funded by the National Natural Science Foundation of China (grant No. 41772387), Natural Science Foundation of Heilongjiang Province (grant No. LH2020E027), and Harbin University of Commerce Industrialization Project Support Plan (grant No. XL0092), China Postdoctoral Science Foundation (No. 2021M690828), Heilongjiang Postdoctoral Grant (No. LBH-Z20145), and Self Planned Task (No. SKLRS202113B) of the State Key Laboratory of Robotics and System (HIT).

Data Availability Statement: Not applicable.

Conflicts of Interest: The authors declare no conflict of interest.

Abbreviations

The following abbreviations are used in this manuscript:

Abbreviation	Meaning
NMS	Neutral mass spectrometer
NMR	Nuclear magnetic resonance technique
T	Trace element temperature
λ	Sample thermal conductivity
C_p	Volumetric heat capacity of the sample
ρ_i	Density of ice
θ_i	Volumetric ice content of the sample element
L	Latent heat of phase transformation
A	Strength of the nuclear magnetic signal
θ_s	Saturated volume moisture content of the sample
ρ_s	Dry density of the sample
ρ_w	Density of water at room temperature

References

1. Benna, M.; Hurley, D.M.; Stubbs, T.J. Lunar soil hydration constrained by exospheric water liberated by meteoroid impacts. *Nat. Geosci.* **2019**, *12*, 333–338. [CrossRef] [PubMed]
2. Kendrick, A.K.; Knight, R.; Johnson, C.D.; Liu, G.; Knobbe, S.; Hunt, R.J.; Butler, J.J., Jr. Assessment of NMR Logging for Estimating Hydraulic Conductivity in Glacial Aquifers. *Groundwater* **2021**, *59*, 31–48. [CrossRef] [PubMed]
3. Taber, S. The mechanics of frost heaving. *J. Geol.* **1930**, *38*, 303–317. [CrossRef]
4. Sill, R.C.; Skapski, A.S. Method for the determination of the surface tension of solids, from their melting points in thin wedges. *J. Chem. Phys.* **1956**, *24*, 644–651. [CrossRef]
5. Hoekstra, P. Moisture movement in soils under temperature gradients with the cold-side temperature below freezing. *Water Resour. Res.* **1966**, *2*, 241–250. [CrossRef]

6. Xu, X.; Wang, J.; Deng, Y. Development of an experimental device for water transport in soil. *J. Glaciol. Geocryol.* **1988**, *2*, 189–196.
7. Peng, Z. *Mechanism and Simulation of Coupled Migration of Water, Heat and Solute in Unidirectional Frozen Soil*; Wuhan University: Wuhan, China, 2015; pp. 120–128. (In Chinese)
8. Kleinhenz, J.; Sacksteder, K.; Nayagam, V. Lunar resource utilization: Development of a reactor for volatile extraction from regolith. In Proceedings of the 46th AIAA Aerospace Sciences Meeting and Exhibit, Reno, Nevada, 7–10 January 2008; p. 1415.
9. Zhu, M.; Song, H.; Zhong, W. Water migration mechanism and treatment measures of roadbed in seasonal freezing area. *Roadbed Eng.* **2007**, *1*, 63–64.
10. Liu, B. *Migration of Water in Soil during Freeze-Thaw Process*; Harbin Institute of Technology: Harbin, China, 2008; pp. 68–72. (In Chinese)
11. Harlan, R.L. Analysis of coupled heat-fluid transport in partially frozen soil. *Water Resour. Res.* **1973**, *9*, 1314–1323. [CrossRef]
12. Heitman, J.L.; Horton, R.; Ren, T. A test of coupled soil heat and water transfer prediction under transient boundary temperatures. *Soil Sci. Soc. Am. J.* **2008**, *72*, 1197–1207. [CrossRef]
13. Xu, J.; Niu, F.; Niu, Y.; Hou, Z. Analysis of water migration characteristics of subgrade soil during freezing process. *J. Chongqing Univ.* **2013**, *36*, 150–158.
14. Hopke, S.W. A model for frost heave including overburden. *Cold Reg. Sci. Technol.* **1980**, *3*, 111–127. [CrossRef]